Materials Research Bulletin 153 (2022) 111873

Contents lists available at ScienceDirect

Materials Research Bulletin

journal homepage: www.elsevier.com/locate/matresbu

Research Papers

From quaternary to senary high entropy antimonide nanoparticles by a facile and scalable thermal treatment method

Nayereh Soltani [a], Jamil Ur Rahman [a], Patricia Almeida Carvalho [b], Calliope Bazioti [a], Terje Finstad [a,*]

[a] Department of Physics, Centre for Materials Science and Nanotechnology, University of Oslo, 0371 Oslo, Norway
[b] SINTEF Materials and Chemistry, 0373 Oslo, Norway

ARTICLE INFO

Keywords:
Intermetallic compounds
Nanostructures
Electron microscopy
X-ray diffraction
Crystal structure

ABSTRACT

Transition metal antimonides form a class of intermetallic compounds, which has drawn considerable attention due to their potential applications in various fields. However, the formation of nanostructures containing multiple transition metal elements has been a challenge. Here, a new class of multicomponent antimonide nanoparticles with chemical composition ranging from quaternary to senary were synthesized via a simple, reproducible, and scalable thermal treatment method. This method allows uniform elemental distributions in a single nanoparticle, demonstrating the ability to obtain medium- and high-entropy antimonide nanostructures. The mechanism of formation was proposed and the characteristics of obtained nanoparticles were investigated by X-ray diffraction, field emission scanning electron microscopy, and high-resolution transmission electron microscopy. Under the achieved optimal synthesis conditions, the formation of a single-phase with a hexagonal structure ($P6_3/mmc$) was observed for the quaternary and quinary samples, whereas in the case of the senary samples, a trace of minor impurity can be observed.

1. Introduction

Alloys are combinations of different metallic elements whose properties are often quite different from those of their individual constituents. New or unique properties are obtained by changing either the constituent elements or by changing the composition. In general, there are two major types of alloys, namely, solid solution alloys and alloys containing intermetallic compounds. Solid solution alloys are random mixtures of metals, typically with a simple stacking of the metal atoms in the crystal structure of one of the constituent elements or in a random amorphous structure [1]. Intermetallic alloys contain compounds with a defined stoichiometry and crystal structure, in which the atoms of the constituent elements are assigned to specific sites [2].

As the number of elements and their concentrations increase in a solid solution alloy, the configurational entropy increases. The large configurational entropy of mixing can yield a reduction in free energy overcoming a possible enthalpy gain by de-mixing or compound formation. This thus stabilizes solid solutions of otherwise immiscible elements in typically simple crystal structures. This entropy stabilization constitutes a novel materials-design paradigm for the realization of new compounds with possibly widely tunable properties [3–7]. Variation in components, stoichiometry, and crystal structure of multicomponent metallic allows for the realization of unique properties and tuning toward a broad range of applications in the fields of catalysis, energy, medicine, and electronics [8–11].

The interest in high entropy alloy (HEA) materials has been growing dramatically in the last decades within fundamental and applied material science [11–15], and many synthesis methods have been developed for synthesizing both bulk and nanoscale HEAs. Synthesis of bulk HEAs currently relies mostly on vacuum arc-melting [14] powder metallurgy, mechanical alloying, and spark plasma sintering [16,17]. The approaches to synthesize HEA nanoparticles (NPs) include carbothermal shock [18], fast-moving bed pyrolysis [19], sol-gel combustion [20], mechanical grinding [21], wet chemistry methods [22–25], ultrasound and laser-synthesis [26–28].

It has been reported that a reduction in the particle size to nanometer scale is expected to improve the properties and increase the application potential of high-entropy alloys [20]. The formation of nano multicomponent intermetallic precipitations in bulk superalloys and HEAs drastically increases their ultimate tensile strengths [29–32]. It seems

* Corresponding author.
E-mail address: terje.finstad@fys.uio.no (T. Finstad).

https://doi.org/10.1016/j.materresbull.2022.111873
Received 16 November 2021; Received in revised form 12 April 2022; Accepted 18 April 2022
Available online 20 April 2022

that some principles behind the stability enhancement of HEA solid solution NPs by entropy can be extended to intermetallic NPs. However, most research groups focus primarily on random HEA NPs, ignoring isolated high entropy intermetallic NPs because substituting the lattice sites of the intermetallic compound by a variety of metals in the nanoscale regime appears more challenging than the same thing for simple solid solutions NPs. Therefore, it is important to work on the development of new strategies for synthesizing high entropy intermetallic NPs to design new compounds with the desired physical properties.

Amongst many intermetallic compounds, transition metal antimonides form an important class that has drawn considerable attention due to their highly stable nature and potential applications in thermoelectrics [33,34], anode material in lithium and sodium-ion batteries [35–37], catalytic activity in hydrogenation [38,39], electrocatalytic activity in hydrogen evolution reaction [40], etc. Among these antimonides are Sb-based half-Heusler compounds [41,42], skutterudites [43] [44], clathrates [45], zintl-antimonides [46], and binary antimonide with NiAs type crystal structure [47–50], which show a wide variety of composition-dependent electrical and magnetic properties that makes them interesting materials in metallurgy and solid-state science.

Nevertheless, forming transition metal antimonides nanostructures containing more than three metal elements using wet chemistry approaches are usually restricted by difficulties arising from balancing the diverse reduction rates of different metal precursors [51]. This often results in site-selective nucleation of each metal and formation of NPs with structures and components varying from particle to particle, especially when incompatible metal elements such as Cu and Co are used.

The studies presented herein verify the feasibility of synthesizing isolated multicomponent/ high entropy antimonide NPs via a simple, reproducible, and scalable thermal treatment method. The remarkable method allows uniform elemental distributions in single NPs with chemical compositions ranging from quaternary to senary. The obtained NPs have a hexagonal structure, which can be described as a hcp arrangement of unary antimony atoms with transition metal atoms filling the octahedral voids randomly to exploit the configurational entropy.

2. Materials and methods

Metal salts of antimony chloride $SbCl_3$ (≥99%), zinc chloride $ZnCl_2$ (≥98%), nickel chloride $NiCl_2{\bullet}6H_2O$ (≥97%), cobalt chloride $CoCl_2{\bullet}6H_2O$ (≥98%), copper chloride $CuCl_2$ (99%), and iron chloride $FeCl_3$ (≥97%) were used as metal precursors. Polyvinyl pyrrolidone (PVP25 with mol wt=25,000 / PVP40 with mol wt=40,000) was used as a stabilizer and capping agent. All chemical reagents were purchased from Sigma-Aldrich and used without further purification. Ethanol (99.96%) was purchased from VWR chemicals and used as a solvent.

A thermal treatment method that has been applied for the synthesis of metal oxide NPs without using any catalyst, and described and discussed elsewhere [52], has been adopted in this work with some modifications. First, because of the reaction of antimony chloride with water, ethanol was chosen as an alternative solvent based on solubility tests for the different metal chlorides. Second, a post-treatment of calcination in the hydrogen atmosphere was added to remove oxygen content.

In a typical procedure, the appropriate amount of PVP was dissolved in ethanol at a temperature of 60 °C under continuous stirring. Subsequently, the designed molar amount of metal chlorides were added to the PVP solution one by one under stirring (500 rpm) followed by ultrasonication for homogenization. The final solution was dispensed into a petri dish and dried in air at 60 °C for 24 h in a controlled environment. The resulting green solid material was crushed and ground into powder, and calcined in a two steps procedure. The first step was carried out in air at a temperature of 600 °C for 2 h to decompose the polymer and to crystallize the metal oxide NPs. The second step of calcination was performed in a hydrogen atmosphere using a ProboStat™ cell (NORECS AS) in a vertical tube furnace at temperatures of 400–510 °C in a retention time of 2–15 h to remove oxygen and obtain transition metal antimonide NPs.

3. Characterization

X-ray diffraction (XRD) characterization was made utilizing the Bruker AXS D8 Discover system. The X-ray source was Cu Kα (λ = 1.5406Å), and a Ge (220) double bounce monochromator was used to filter out the $K\alpha_2$ signal (λ = 1.5444Å). XRD analysis was done using the powder difracrion files (PDF) found in the Inorganic Crystal Structure Database (ICSD) [53]. Surface morphology analysis of products was performed by scanning electron microscopy (SEM) using a field emission microscope (FEI Quanta 200 FEG SEM). The average size and size distribution of the NPs were evaluated from at least 100 NPs for each sample in high resolution images. The compositional analysis was carried out using energy-dispersive X-rays (EDX) spectroscopy by an attachment to SEM instrument. High-resolution scanning transmission electron microscopy (HR-STEM) with EDX was employed using a probed-corrected FEI Titan G2 60–300 microscope operated at 300 kV. The samples were suspended in ethanol and put onto a gold grid. The chemical interaction of PVP with NPs was investigated using a Fourier Transform Infrared (FTIR) Spectrometer (Nicolet Summit).

4. Results and discussion

A proposed mechanism for the synthesis of multi-component transition metal antimonide NPs using the thermal treatment method is schematically shown in Fig. 1. In the first step of making the initial solution, PVP works as a stabilizer or a mediator for dissolving metallic salts through steric and electrostatic stabilization of the pyrrolidone rings (amide functions) and methylene groups. By dissolving metal chlorides in the PVP solution, the stable complexes are formed by strong ionic bonds between the amide group of polymeric chains and metallic ions. These mechanisms terminate by loss of solvent in the drying step. After drying, the uniform immobilization of metallic ions in the cavities of the polymer chains permits local stoichiometry and favors the formation of uniformly distributed metal oxide solid solution NPs in the calcination process [52].

The influence of PVP is not restricted to the liquid medium and drying step; PVP also affects the formation of the nuclei in the first step of calcination. The combined stabilizing and surface protecting properties of PVP prevented the NPs from uncontrolled growth and agglomerating, and initial multi-metallic oxides form inside the porous carbonaceous matrix. Thermal degradation of PVP takes place at around 480 °C and emits gasses such as CO, or CO_2, NO, and water vapor that maintain the combustion energy loss and prevent the aggregation of small particles [54]. Hence, the calcination step in air should be carried out at a temperature higher than 500 °C to ensure decomposition of the polymer as well as reduction and coalescence of the aggregate metal ion precursors into a single NP. The second step of calcination is carried out under flowing H_2, which results in the reduction of multi-metallic oxide NPs into multicomponent transition metal antimonide NPs. Due to the elimination of the polymer in this stage, it is difficult to obtain well separated, monodisperse NPs. However, the small particle size of the reactants and low reaction temperatures ensure the formation of nanosized particles.

Based on the literature reports on the synthesis of binary NiSb, CoSb, and FeSb [48], attempts were made primarily to synthesis quaternary $(NiCoFe)Sb_3$ NPs, and then we tried to introduce additional elements of Cu and Zn into the structure. These five dissimilar transition elements, Ni, Co, Fe, Cu, and Zn, have a range of reduction potentials, −0.76 V to 0.34 V, versus the standard hydrogen electrode. They have atomic radii of 1.24 Å to 1.33 Å, and melting temperatures of 420 °C to 1535 °C.

Since no prior synthesis of these compounds has been reported, we determined optimum conditions by investigating the influence of several

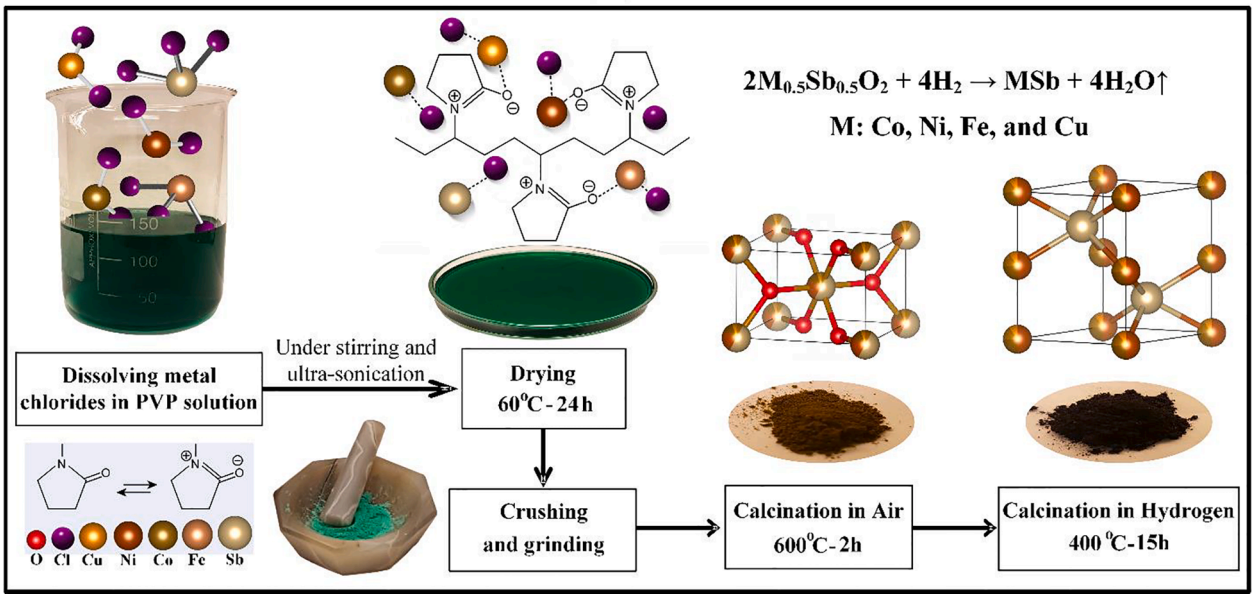

Fig. 1. Schematic representation of synthesis and mechanism of formation of quinary antimonide NPs.

parameters: concentration and molecular weight of PVP, calcination time and temperature, the initial composition of the elements, heating and cooling rate, and hydrogen flow. The products were examined before and after different synthesis steps by XRD, SEM, HR-STEM, and EDX. The synthesis conditions for the formation of different antimonides were optimized in terms of particle size and distribution, oxygen removal, phase purity, and crystallinity.

To understand the role of PVP molecular weight, and to determine the required amount of PVP in the reactions, a series of samples containing 50 at.% Sb and equimolar proportions of the other elements were synthesized using PVP25 and PVP40 by varying the molar ratio of PVP to metal chlorides (i.e., 0, 0.5, 1, and 1.5). The molar concentration of PVP was calculated in terms of the repeating unit of PVP with a molecular weight of 111.14 g/mol. The results show that both PVP molecular weight and concentration affect the size distribution and dispersion of the resulting NPs, especially in the first step of calcination. Fig. 2 shows representative SEM images and corresponding size distribution histograms of multi-metallic oxide NPs synthesized with different PVP molecular weights and concentrations. The high resolution images were used for evaluation of particle sizes. As can be seen in Fig. 2(a), in the absence of PVP, despite using a lower temperature and shorter calcination time, the sample contains agglomerated particles with non-uniform shapes and relatively large sizes, which can promote the growth of particles in the second step of calcination.

Conversely, the presence of PVP leads to the formation of spongy and fragile material with pores and voids that are attributed to the release of gasses during the decomposition of PVP. At low PVP concentrations (Fig. 2(b)), the polymer cannot entirely cover the metal ions, and consequently, agglomerated particles with quite large sizes and broad size distribution are produced. However, with PVP, the NPs become more regular in shape than they are for the case without PVP.

When the molar ratio of PVP to metal chlorides is increased to 1, more ions can be covered by the polymer. Thereby the size of the NPs decreases and monodispersed particles are obtained for both PVP25 and

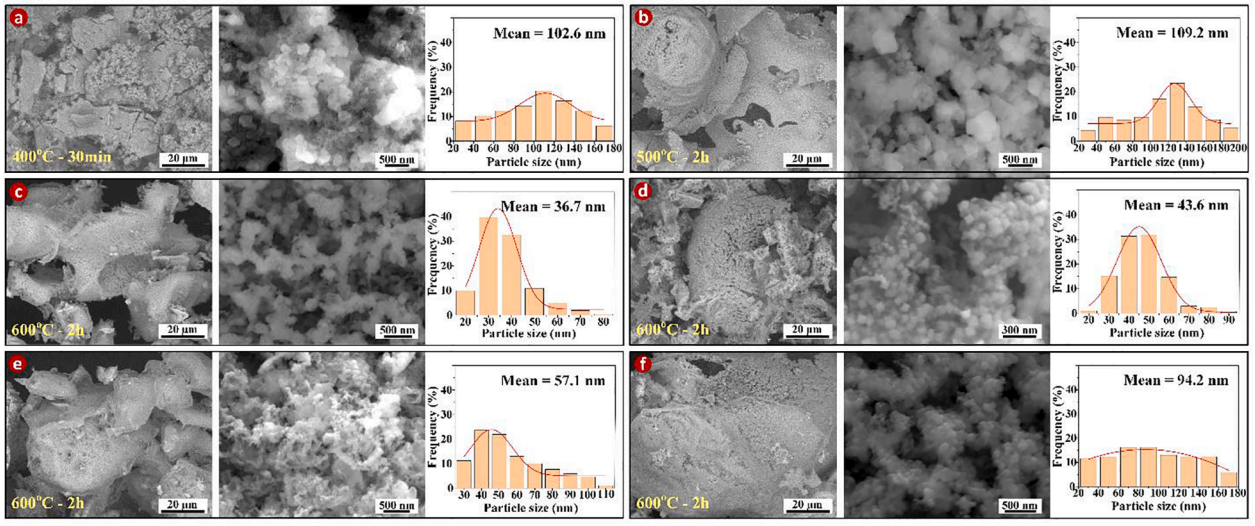

Fig. 2. SEM images (high and low magnification) and corresponding particle size distribution histograms with Gaussian-fitteng curve (solid line) of the synthesized sample (a) in the absence of PVP, and with PVP25 and molar ratio of polymer to chloride of (b) 0.5, (c) 1, and (d) 1.5, and with PVP40 and molar ratio of (e) 1, and (f) 1.5.

PVP40 and the surface morphologies are quite similar. Nevertheless, the NPs obtained with PVP25 are smaller than those prepared with PVP40 and have a narrower size distribution (Fig. 2(c) and 2(e)). In particular, polymers with higher molecular weights can provide stronger adsorption and better stabilization due to their lesser freedom of motion. However, from the contrary results, we conclude that the amount of metal ions that can be coverd by polymer in these cases is directly proportional to the number of PVP chains.

With a further increase of PVP25 (Fig. 2(d)), well isolated and monodispersed particles were obtained at the expense of increased particle size. The increase in particle size might be caused by the accumulation of small NPs with excess PVP [55] and the growth of primary NPs due to the Ostwald ripening phenomenon.

In contrast, with increasing PVP40 concentration (Fig. 2(f)), the size of the NPs increases noticeably and a very broad size distribution is obtained. The difference can be attributed to the larger polymer chains and stronger steric effect of PVP40. Those differences make it more difficult for the polymer to adsorb the metal ions. It was observed that the metal chlorides are dissolved in PVP40 solution for longer ultrasonication time than the case for PVP25.

Generally, the particle nucleation and growth kinetic determines the final NP size [56] and the monodispersed particles are favorably formed when the rate of nucleation is much higher than the growth rate [57]. According to the obtained results, PVP25 with a molar concentration of ~1.2 was selected as the optimum for the rest of the experiments. These values for the molecular weight and concentration are the key parameters for the efficient binding of PVP and metal ions, and can provide the kinetic conditions required to fabricate well dispersed NPs with a sufficiently small mean size and narrow size distribution.

The reported reaction temperatures and time for the above-mentioned samples are the lowest possible ones allowing the chlorine removal (in the absence of PVP) and complete decomposition of PVP. To ensure PVP decomposition, FTIR analysis of the samples was carried out and the obtained data were compared to the FTIR spectra of the pure PVP and the synthesized sample in the absence of polymer. As shown in Fig. 3, the dominant absorption peaks of polymers corresponding to functional O—H, C—H, C = O, and C—N bands were completely removed for all samples after calcination in air at temperature up to 600 °C. The observed peaks for wavenumbers lower than 850 cm^{-1} are similar to the peaks of the synthesized samples in the absence of polymer and can be attributed to transition metal-oxide bands [58].

To optimize the temperature and time in the first step of calcination (in air), a series of quinary samples containing 50 at.% Sb and equimolar proportions of other elements (Ni, Co, Fe, and Cu) were synthesized with a sufficient amount of polymer for different calcination temperatures ranging from 500 to 800 °C and different calcination times ranging from 2 to 4 h. Fig. 4 shows the SEM images and XRD patterns of samples calcined in air at different temperatures for 2 h. As illustrated in the SEM images, by increasing the calcination temperature, the spongy and fragile form of the samples decreases in extent and agglomerated particles with larger sizes are produced. This can be attributed to the rapid decomposition of the polymer at high temperatures. As a result, in the absence of polymer at the highest reaction temperature, the particles can fuse together and form larger particles.

The observation of sharp peaks in the XRD pattern (Fig. 4(b)) indicates high crystallinity of the products. In all samples, the dominant diffraction peaks match those listed for the tetragonal rutile-type compound $(FeSb)O_4$ (ICSD PDF No 01–074–4589) which is found in the mineral called squawcreekite. This compound has the crystallographic symmetry $P4_2/mnm$ and spacegroup 136. Sb and Fe occupy the metal site in this structure with no ordering. The compound is then a pseudo-solid-solution of FeO_2 and SbO_2 with rutile structure. It is feasable that all the transition metals used here could enter in similar pseudo-solid-solutions. The minor diffraction peaks in Fig 4(b) are related to a cubic lattice and space group 227 with $Fd\bar{3}m$ symmetry and are from impurity phases (possibly spinel-type, Co_3O_4 structures). By increasing the temperature, the intensity and number of the impurity peaks increases. Similar results were obtained by increasing the calcination time. Analysis of the peak broadening (using the Scherrer equation) provides an estimate of the average crystallite size. Other broadening effects such as strain are not accounted for in this analysis, but importantly, the data provide very reliable estimates of the relative changes. The average crystallite size with respect to calcination temperature indicates growth in all directions. From 500 to 700 °C, a linear increase in size with a temperature coefficient about 0.02 nm/ °C can be observed in all directions, but from 700 to 800 °C, the temperature coefficient dramatically increases in some directions up to ~0.10 nm/ °C. This causes the crystalites to become increasingly elongated in those directions.

Analogous experiments were performed for the senary samples and similar results were obtained. Taking into account the various parameters, the lowest calcination temperature and time of 600 °C and 2 h were chosen as the optimum ones in the first step of calcination (in air) for all samples.

The calcination conditions in the second step (in hydrogen) depend

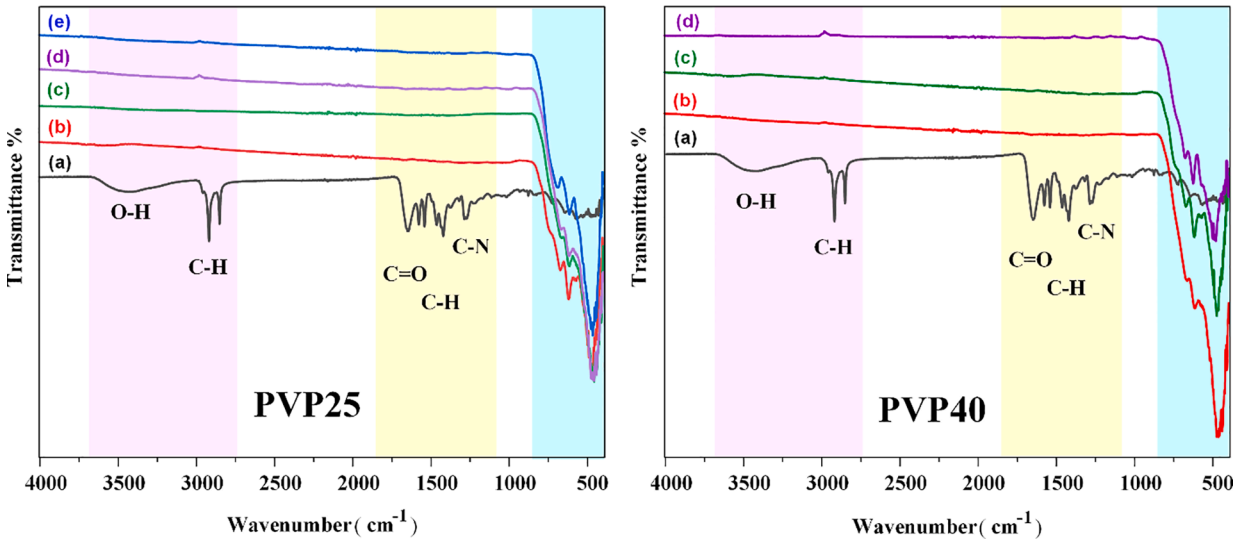

Fig. 3. FTIR spectra of (a) PVP, and synthesized samples with PVP molar ratio (of polymer to chloride) of (b) 0.5, (c) 1, (d) 1.5, and synthesized sample (e) in the absence of PVP.

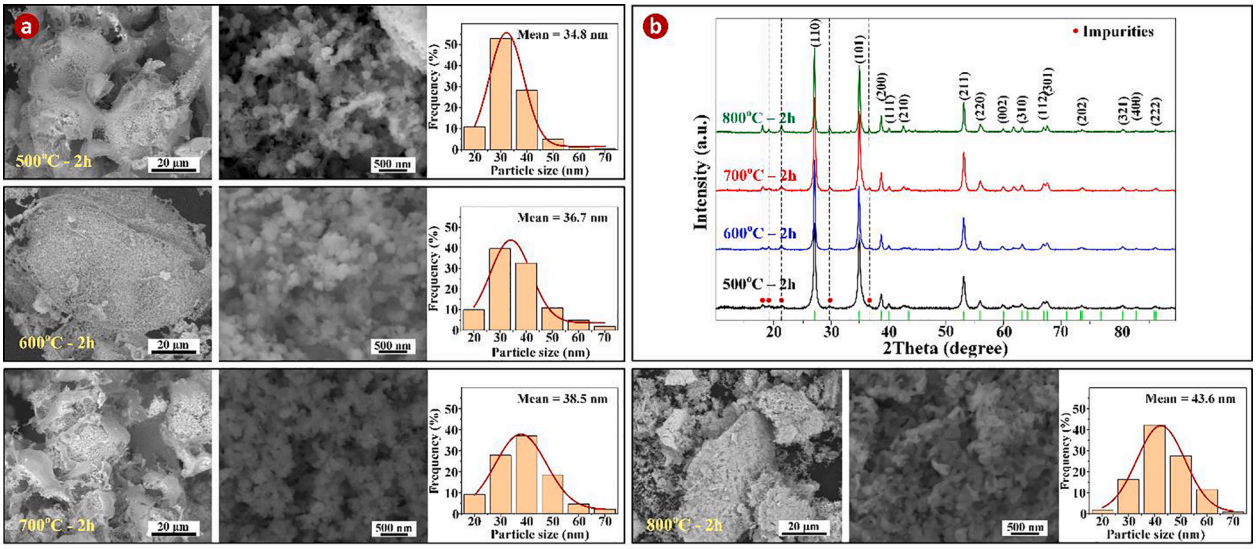

Fig. 4. (a) SEM images (high and low magnification) and corresponding particle size distribution histograms with Gaussian-fitteng curve (solid line) and (b) XRD patterns of quinary samples containing 50 at.% Sb and equimolar portions of other elements (Ni, Co, Fe, and Cu) calcined at different temperatures for 2 h in air. The planar indexing annotated above the XRD peaks are for the tetragonal structure $(FeSb)O_4$ ($P4_2/mnm$) and the positions are indicated as green bars. (For interpretation of the references to colour in this figure legend, the reader is referred to the web version of this article.)

strongly on the composition of the sample. In the quaternary and quinary samples, the oxygen content can be completely removed after heating at a relatively low temperature of 400 °C in a constant hydrogen flow whereas for the senary sample, a higher temperature is needed, as will be discussed in detail later.

The quaternary sample with a nominal composition of 50 at.% Sb and equimolar proportions of the other elements (Ni, Co, and Fe) was prepared using a sufficient amount of polymer and calcined in air under the achieved optimal conditions of 600 °C and 2 h. In the second step of calcination in hydrogen, low temperature is preferred to ensure the formation of nanosized particles in the absence of polymer. In contrast, to achieve full conversion of metal oxides to metal antimonides, a relatively long reaction time is required to allow the constituent metals to adopt a stable configuration (based on element compatibility). The optimal calcination temperature and time for this particular sample were found to be 400 °C and 15 h, respectively. EDX mapping in SEM for this sample shows that each of the elements is homogeneously distributed throughout the entire sample. The metal ratios in the sample reflect metal ratios in the precursor solution and tell that the composition of the final products can be tuned by simply adjusting the ratio of metal salts in the precursor solution. As shown in Fig. 5, the XRD profiles of the calcined sample in both air and hydrogen do not show any peaks corresponding to impurities, indicating the formation of the single-phase NPs. All the XRD peaks of the calcined sample in air can be accurately indexed to a pure-phase of the tetragonal structure of space group 136 ($P4_2/mnm$) corresponding to $(FeSb)O_4$ structure. The estimated crystallite size of the oxide NPs using the (110) reflection of the XRD patterns and the Scherrer equation, is 25.7 nm. The XRD pattern of the calcined sample in hydrogen shows a series of sharp and well-defined peaks associated with a single-phase hexagonal structure in space group 194 ($P6_3/mmc$) corresponding to the NiAs structure (nickel arsenide). The estimated crystallite size of antimonide NPs derived from the (101)

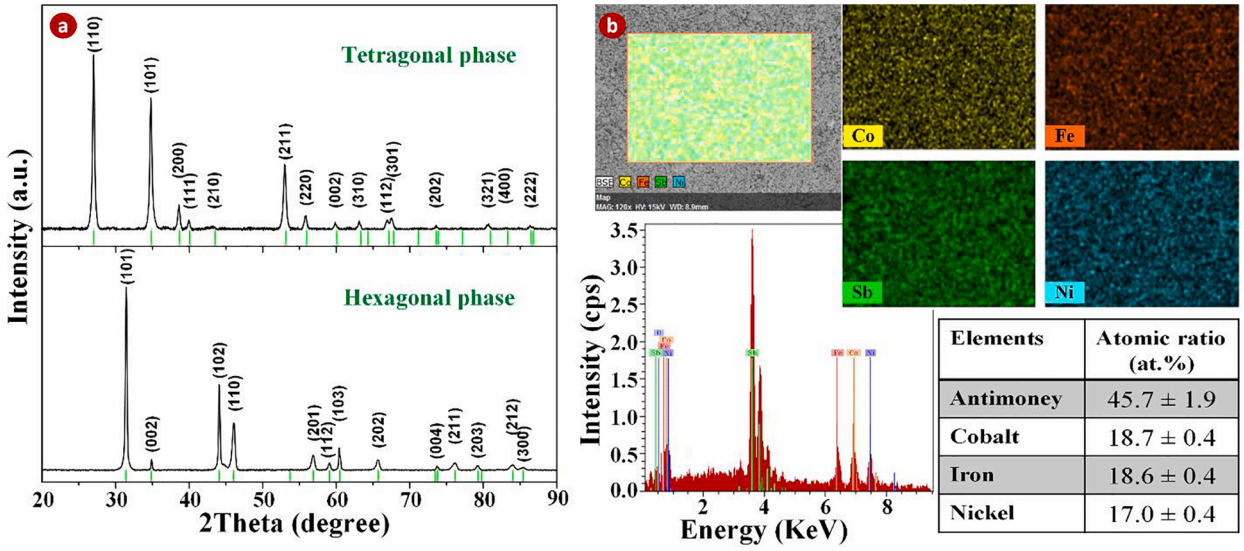

Fig. 5. (a) XRD patterns of the quaternary sample (top) after calcination in air at 600 °C for 2 h yielding a tetragonal $(FeSb)O_4$ structure and (bottom) after calcination in hydrogen at 400 °C for 15 h yieldining a hexagonal NiAs structure. (b) SEM image and EDX maps of quaternary sample after calcination in hydrogen with corresponding EDX spectrum and quantities analysis.

reflection of the XRD patterns is 32.3 nm. These results show that the synthesized quaternary NPs are atomically mixed without any phase segregation. The formation of multicomponent compounds from metal salt or metal oxide precursors necessarily involves the reduction of the metals, and it is difficult to reduce the precursors of four different metals (Ni, Co, Fe, and Sb) simultaneously and merge them into a homogenous NP. Nevertheless, phase control is possible for these systems because the initial core structure is thermodynamically favorable, and the polymer provides the local stoichiometry during the drying step.

From the Boltzmann-Planck equation for entropy in statistical mechanics, the molar configurational entropy, ΔS_{mix}, of a crystalline material containing n different metal atoms in solution is given by the following Eq. [5,20]:

$$\Delta S_{mix} = -R\sum_{j=1}^{n} x_j ln(x_j) \quad (1)$$

where R is the gas constant (8.314 J/K mol) and x_j is the fraction of available lattice sites for occupancy of metal atoms of type j. In the case of multicomponent antimonides with NiAs structure, the Sb atoms are located in the As sublattice sites, with a molar fraction of 1, while the Ni sites in the structure can be occupied randomly with the other transition metal atoms. Hence, the configurational entropy of quaternary antimonide NPs considering $n = 4$, x_{Sb}=1, x_{Co}=18.7/54.3, x_{Fe}=18.6/54.3, and x_{Ni}=17.0/54.3 (Fig. 5) is ΔS_{mix}=1.1R. Based on some classifications of solid solutions in the literature [15,59], the ΔS_{mix} calculated above is consistent with the value for a medium entropy alloy (MEA). In reality, the entropy of mixing may be larger because it will also have contributions from vibrational, magnetic, and electronic entropy [60,61]. For compunds, there are also other parameter combinations that are suggested as descriptors indicating the stability of compounds [62], but the configurational entropy is important.

For quinary samples synthesized with a nominal composition of 50 at.% Sb and equimolar proportions of the other elements (Ni, Co, Fe, and Cu), it is observed that the optimal calcination conditions (Alloy 5–1) produce major crystallographic phases which are the same as those for the quaternary sample. The strongest lines shown in Fig. 4(b) are from the tetragonal phase (rutile type, $P4_2/mnm$ symmetry, and space group 136). The configurational entropy of this phase would be higher for quinary samples than for quaternary samples, and the free energy would be less for the quinary sample if a rutile type pseudu-solid-solution is formed. That would be favorable for the production of quinary samples. The dominant diffraction peaks in the XRD profiles of Alloy 5–1 in Fig. 6 (b) can be indexed as the hexagonal phase ($P6_3/mmc$ symmetry, and space group 194) which is in accordance with the observed phase in the quaternary sample. The formation of minor impurities for both calcined samples in air (Fig. 4) and in hydrogen (Fig. 6) indicate that entropy alone does not explain the observed product distributions in the intermetallic compounds and the kinetics of the reduction reaction and the thermodynamics of product formation may be more important for determining the product distributions.

Copper has the highest standard reduction potential among the metal elements in the quinary samples, and, consequently, was reduced preferentially at the beginning of the reaction. The resulting overabundance of copper monomers during the early part of the reaction could result in the production of copper-rich compounds, which would also affect the product composition over the course of the reaction. Moreover, the enthalpy of mixing of Cu with the other three elements (Ni, Co, and Fe) is positive, while those between the other three elements are negative. So, the difficulty of mixing Cu with other elements is leading to less contribution of the Cu element in the main phase [12]. Accordingly, attempts were made to minimize impurities in the product by varying the nominal composition of samples (Table 1). First, by decreasing the initial atomic percentage of copper to 7.5 and increasing the atomic percentage of nickel and cobalt to 15 (Alloy 5–2). This reduces the amount of copper-rich phase but leads to the formation of iron-rich phase as the second impurity (Fig. 6) which is likely due to competing kinetics. Another sample was prepared by adjusting the initial molar ratio according to the average atomic composition obtained from the EDX-STEM analysis of the main phase NPs (Alloy 5–3). The obtained result for this sample was similar to the previous one. Finally, the initial composition of 50 at.% Sb, 25 at.% Ni, 12 at.% Co, 8 at.% Fe and 5 at.% Cu was selected as the optimal combination (Alloy 5–4) which can produce almost a single-phase product by applying the fast heating and quenching rates in hydrogen reduction to prevent the multicomponent NPs from reaching their favorable thermodynamically phase-separation state [11]. The estimated crystallite sizes of antimonide NPs in different

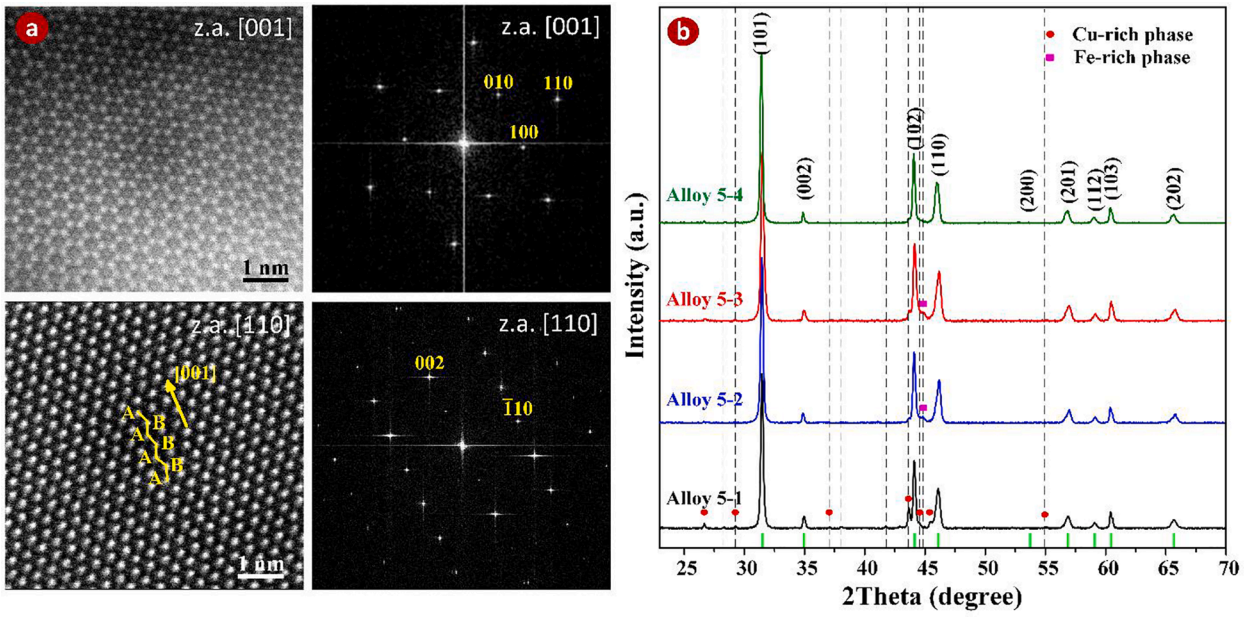

Fig. 6. (a) High-resolution HAADF-STEM images of the quinary antimonide NPs (main phase) and the corresponding fast Fourier transform (FFT) diffractograms along the [001] and [110] zone axes of the hexagonal structure. (b) XRD patterns of quinary samples with different compositions synthesized under the optimal calcination conditions. The planar indexing annotated above the XRD peaks are for the hexagonal ($P6_3/mmc$) NiAs structure (main phase) and the positions are indicated as green bars. (For interpretation of the references to colour in this figure legend, the reader is referred to the web version of this article.)

Table 1
The nominal atomic percentage of elements in the quinary samples, the crystallite size of the main phase derived from the (101) reflection of the XRD patterns and lattice parameters.

sample	The nominal atomic percentage of elements					Crystallite size(nm)	Lattice parameters	
	Sb (at.%)	Ni (at.%)	Co (at.%)	Fe (at.%)	Cu (at.%)		ɑ (A°)	c (A°)
Alloy 5–1	50.0	12.5	12.5	12.5	12.5	38.8	3.934	5.126
Alloy 5–2	50.0	15.0	15.0	12.5	07.5	33.4	3.926	5.151
Alloy 5–3	48.6	17.7	15.5	09.7	08.5	34.8	3.933	5.163
Alloy 5–4	50.0	25.0	12.0	08.0	05.0	35.4	3.942	5.134

quinary samples from the (101) reflection of the XRD patterns and lattice parameters are listed in Table 1 showing a slight difference depending on composition.

As shown in Fig. 6, the dominant crystal phase for all quinary antimonide samples is hexagonal NiAs structure with a high degree of crystallinity, which is further confirmed by high angle annular dark field STEM (HAADF-STEM) imaging and the corresponding FFT diffractograms along the [001] and [110] zone axes. The arrangement of atoms in this structure can be described by the A-B-A-B stacking sequence along the [001] direction in which it consists of unary antimony atoms in a hexagonal close-packed structure with the transition metal atoms randomly distributed in the octahedral voids (Fig. 1). The copper-rich phase has a tetragonal structure corresponding to Cu_2Sb and the iron-rich phase has a cubic structure corresponding to Fe.

Further analysis was performed on the quinary antimonide samples by EDX in STEM-mode of individual NPs to investigate the elemental distribution within a single NP in the samples (Fig. 7). The result is a homogeneous distribution of all five elements in the entire NP of the main phase. The average atomic fractions of the five elements extracted from EDX mapping of different regions shown in Fig. 7 are tabulated in Table 2. It shows the minor contribution of Ni, Co, and Fe in the Cu-rich phase and Ni in the Fe-rich phase.

The STEM image of a large area of the optimal quinary sample (Alloy 5–4) along with EDX mapping of the elements provided in Fig. 8 reveal that all NPs contain all five elements. EDX maps showed that Sb, Ni, Co, and Cu exhibit similarity in their distribution, however, the distribution

Table 2
The quantitative EDX-STEM analysis of different mapping regions shown in Fig. 7.

	Sb (at. %)	Ni (at. %)	Co (at. %)	Fe (at. %)	Cu (at. %)
Main phase (1)	47.77	17.19	13.30	09.49	12.24
Main phase (2)	49.31	16.30	13.98	12.78	07.73
Cu-rich phase (3)	40,50	03.00	00.70	03.60	52.20
Fe-rich phase (4)	16.97	01.70	06.40	62.48	12.45

of Fe is slightly different. To have a more detailed understanding of the distribution of elements, mixed EDX map of Ni and Fe and line scan across a region of interest have been performed for this sample. The mixed EDX shows that the distribution of Ni and Fe is similar except for at some small points at the boundaries showing the formation of very tiny Fe-rich grains. The line scan confirmed that all the elements are evenly distributed through the particles following the target composition with a small deviation for Fe on the surface of the NPs. The average atomic percentage of the elements determined by the quantitative EDX analysis are in good agreement with the nominal percentage of the elements. Based on the EDX analysis of the main phase NPs in different quinary samples, the configurational entropy of quinary antimonide NPs were calculated to be in the range of 1.2*R* to 1.4*R*, which are classified as MEAs [15,59]. The presence of the sixth element in the NPs can increase

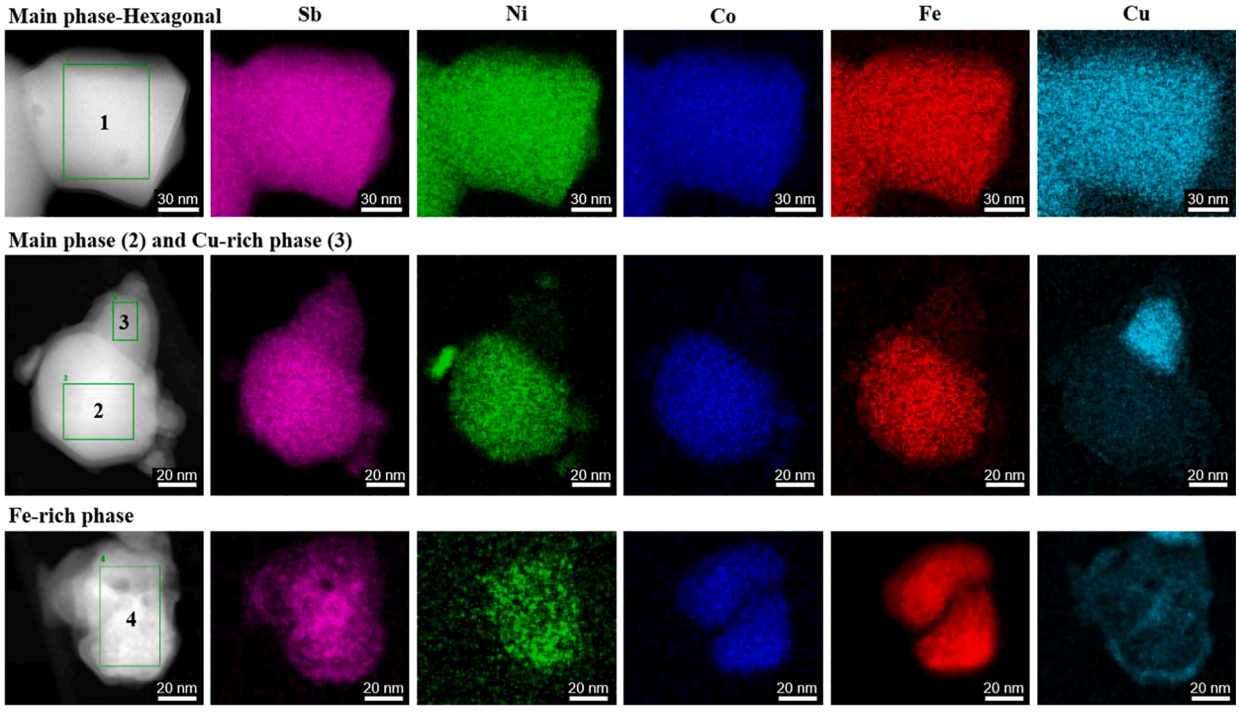

Fig. 7. STEM images and their corresponding EDX maps of individual NPs of the main-hexagonal phase, Cu-rich phase, and Fe-rich phase in the non-optimized quinary samples.

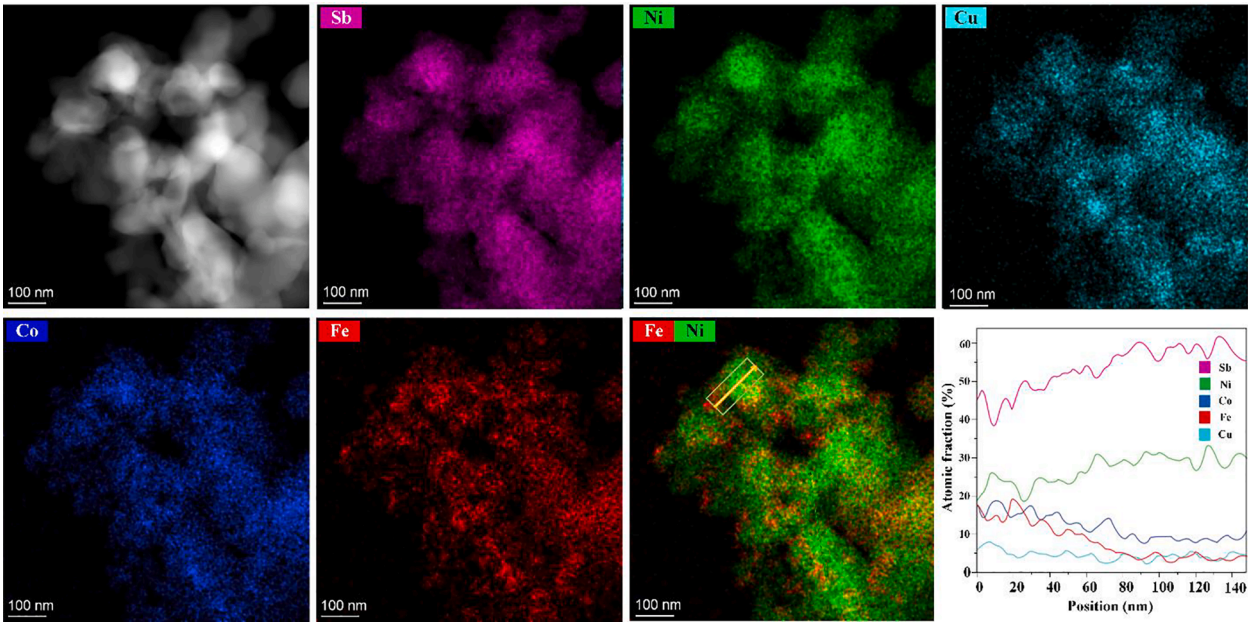

Fig. 8. HAADF-STEM image and its corresponding EDX maps and EDX line scan of the optimal quinary sample (Alloy 5–4).

the entropy further and possibly enhance the stability of antimonide NPs [3].

The first senary sample was prepared with a nominal composition of 50 at.% Sb and equimolar percentages of the other elements (Ni, Co, Fe, Cu, and Zn). It used a sufficient amount of polymer and was calcined in air at 600 °C for 2 h similar to the previous samples. However, due to the high stability of zinc oxide compounds and the volatile nature of zinc, the second step of calcination (in hydrogen) cannot function at 400 °C for 15 h, but requires a quite higher temperature and shorter time. At calcination temperatures below 510 °C, the oxygen content cannot be completely removed and at a higher temperature, the zinc content is evaporated away. In addition, at temperatures between 450 and 510 °C, copper-zinc compounds are formed. Further, at temperatures between 400 and 450 °C, copper and cobalt-rich compounds, corresponding to Cu_2Sb and $CoSb_3$ structures are formed as impurity phases. Thus, the calcination temperature and time for this sample were selected to be 500–510 °C and 2–2.5 h, respectively. Moreover, since the volatile element of Zn is involved in the synthesis, a precursor compensation approach to balance the atomic ratio of Zn (i.e., add more of Zn component) was employed and the calcination of samples was done in a stagnant hydrogen atmosphere without flow. The dominant phase in senary samples is the hexagonal ($P6_3/mmc$) phase similar to quaternary and quinary samples and zinc oxide impurities are present in all samples because the calcination temperature does not exceed 510 °C to prevent zinc loss.

Further optimization to minimize impurities in the product was performed by varying the nominal composition of samples (Table 3). First, by increasing the molar percentage of nickel to 20 and decreasing the initial concentration of other elements to 7.5 at.% (Alloy 6–2). This reduces the amount of copper-zinc compound but leads to the formation of copper-rich phase corresponding to Cu_2Sb as the other impurity phase (Fig. 9). Moreover, the content of oxygen in this sample is 12 at.% which is a relatively large amount compared to the zinc content. Another sample was prepared by further decreasing the Cu and Zn initial molar ratio (Alloy 6–3). In addition to the main phase and ZnO, an extra peak is observed in the XRD pattern of this sample. The content of oxygen in this sample is 4.5 at.%, which is comparable with the zinc amount and confirms the low contribution of Zn in the main phase. Finally, by re-increasing the zinc amount, the initial composition of 50 at.% Sb, 16 at.% Ni, 10 at.% Co, 7 at.% Fe, 7 at,% Cu, and 10 at.% Zn was selected as the optimal combination (Alloy 6–4) showing only ZnO as an impurity. The estimated crystallite sizes of antimonide NPs in different senary samples from the (101) reflection of the XRD patterns (Table 3) are in the range of 31.6 to 42.5 nm depending on composition and calcination temperature and time. The lattice parameters also show a slight difference depending on composition.

The STEM image of a large area in the optimal senary sample (Alloy 6–4) is shown in Fig. 9 along with EDX mapping of the elements.They reveal that all the NPs contain all six elements but their distribution is somewhat different. EDX mapping of Sb and Cu exhibit a homogeneous distribution of these elements throughout the entire sample, which is consistent with the line scan results. Ni and Co maps show a similar trend. The distribution of those elements are correlated. The NPs that are Ni-rich are also Co-rich. The distribution of Fe, on the other hand, shows a complementary distribution to that of Ni and Co. NPs that are rich in Ni and Co have less Fe and vice versa. This can be seen in the mixed EDX maps of Fe and Ni as well as the line scan diagram and is attributed to the concentration dependence of the enthalpy (if kinetic effects can be ignored). The EDX map of Zn is completely different than those from the other elements, which is due to the formation of ZnO impurity in the

Table 3
The nominal atomic percentage of elements in the senary samples, the crystallite size of the main phase derived from the (101) reflection of the XRD patterns and lattice parameters.

Sample	The nominal atomic percentage of elements						Crystallite size (nm)	Lattice parameters	
	Sb(at.%)	Ni(at.%)	Co(at.%)	Fe(at.%)	Cu(at.%)	Zn(at.%)		a(A^o)	c(A^o)
Alloy 6–1	50.0	10.0	10.0	10.0	10.0	10.0	31.6	3.954	5.137
Alloy 6–2	50.0	20.0	07.5	07.5	07.5	07.5	34.4	3.960	5.158
Alloy 6–3	50.0	20.0	10.0	08.0	06.0	06.0	36.1	3.945	5.131
Alloy 6–4	50.0	16.0	10.0	07.0	07.0	10.0	42.5	3.952	5.136

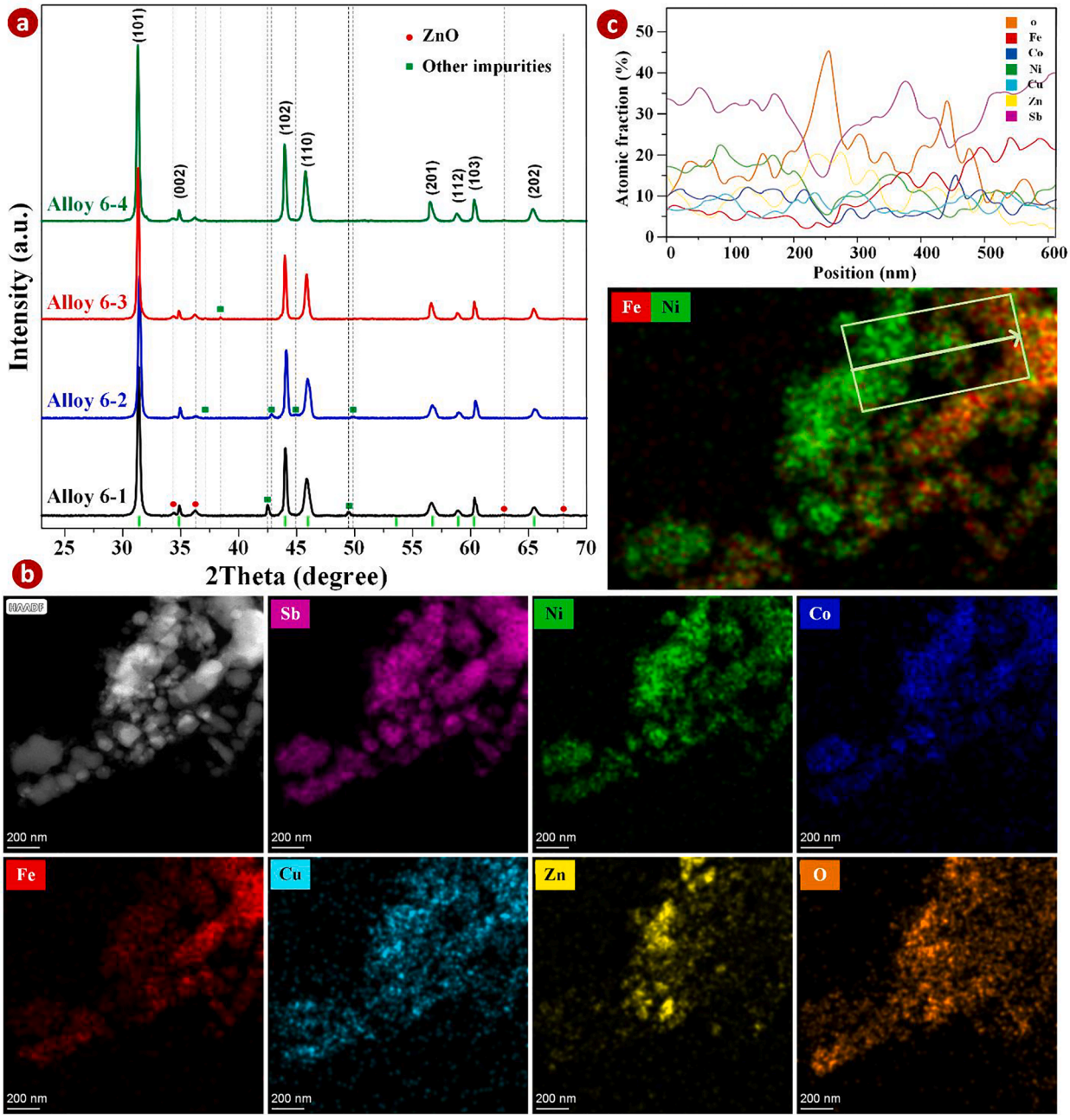

Fig. 9. (a) XRD patterns of senary samples of Alloy 6–1 and Alloy 6–2 calcined at 500 °C for 2 h, and Alloy 6–3, and Alloy 6–4 calcined at 510 °C for 2.5 h. The planar indexing annotated above the XRD peaks are for the hexagonal (P63/mmc) NiAs structure (main phase) and the position is indicated as green bars. (b) HAADF-STEM image and its corresponding EDX maps and (c) EDX line scan of the optimal senary sample (Alloy6–4). (For interpretation of the references to colour in this figure legend, the reader is referred to the web version of this article.)

sample. The overall EDX analysis reveals uniform elemental distributions in single senary antimonide NPs, but the composition of NPs varies from particle to particle.

The calculated configurational entropy of senary antimonide NPs based on quantitative EDX analysis is in the range of 1.4*R* to 1.6*R*, which are classified as MEA and HEAs [15,59].

The possibility of introducing other elements to this nanostructure using the proposed method depends strongly on the stability of their oxide phases. The oxides of the selected elements must be reduced under hydrogen at a relatively low temperature to ensure the formation of NPs. For instance, transition metal elements such as Mn and Cr, which have highly stable oxide phases, cannot be used in this method. The Mn and Cr oxides require high reduction temperatures of 650 and 850 °C, respectively, which lead to surface melting and penetration of NPs to each other to form bulk materials. However, this method can be used for synthesizing a wide range of intermetallic and oxide nanoparticles with multinary composition and large potential for applications in different fields and can be easily upscaled to industrial applications.

Finally, to verify the robustness of the present thermal treatment method, the reproducibility was tested by duplicate syntheses of optimal samples under identical conditions and confirmed by XRD analysis. In addition, XRD and EDX-SEM analysis of various samples were re-recorded after several months of storage under normal conditions (ambient temperature in the dark) to determine the stability of NPs. No significant changes were observed in the characteristics of the samples and their oxygen content after prolonged storage.

5. Conclusion

We have demonstrated a thermal treatment technique towards scalable synthesis of isolated medium/high entropy antimonide NPs with atomic-level mixing of metal elements in a hexagonal NiAs type structure. The elemental distributions are uniform in a single antimonide NP but the composition varies somewhat from particle to particle.

The synthetic reactions involve a complex competition between the thermodynamics of the different product species. However, by careful control of the reaction conditions and initial composition; single-phase antimonide NPs can be obtained. We believe that this facile thermal treatment synthesis technique is a powerful strategy, has enough flexibility to achieve a multitude of multicomponent/high entropy intermetallic and oxide NPs, and has the potential to transcend fundamental research to industrial applications.

Declaration of Competing Interest

The authors declare that they have no known competing financial interests or personal relationships that could have appeared to influence the work reported in this paper.

Acknowledgements

All persons who have made substantial contributions to the work reported in the manuscript, but who do not meet the criteria for authorship, are named in the Acknowledgements.

The authors thank O. B. Karlsen for helping with the XRD measurements and analysis. The authors also thank T. Norby for useful discussions on thermodynamic of chemical reactions and A. M. Dayaghi for his assistance in conducting hydrogen reduction experiments.

The authors acknowledge the Research Council of Norway for financial support through the

NEAT Project No. 262339, ANSWER Project No. 280545, and NORTEM Project No.197405. This work made use of instruments in the Structure Physics and Electrochemistry Lab at Oslo Science Park.

References

[1] K. Kobayashi, K. Kusada, D. Wu, N. Ogiwara, H. Kobayashi, M. Haruta, H. Kurata, S. Hiroi, O. Seo, C. Song, et al., Crystalline to amorphous transformation in solid-solution alloy nanoparticles induced by boron doping, Chem. Commun. 56 (2020) 12941–12944.

[2] E. Antolini, Alloy vs. Intermetallic compounds: effect of the ordering on the electrocatalytic activity for oxygen reduction and the stability of low temperature fuel cell catalysts, Appl. Catal. B. 217 (2017) 201–213.

[3] D. Wu, K. Kusada, T. Yamamoto, T. Toriyama, S. Matsumura, S. Kawaguchi, Y. Kubota, H. Kitagawa, Platinum-group-metal high-entropy-alloy nanoparticles, J. Am. Chem. Soc. 142 (2020) 13833–13838.

[4] M.P. Singh, C. Srivastava, Synthesis and electron microscopy of high entropy alloy nanoparticles, Mater. Lett. 160 (2015) 419–422.

[5] Z. Deng, A. Olvera, J. Casamento, J.S. Lopez, L. Williams, R. Lu, G. Shi, P.F. P. Poudeu, E. Kioupakis, Semiconducting high-entropy chalcogenide alloys with ambi-ionic entropy stabilization and ambipolar doping, Chem. Mater. 32 (2020) 6070–6077.

[6] C.-.C. Tseng, C.-.C. Chi, H.-.J. Tsai, J.-.W. Yeh, H. Ouyang, W.-.K. Hsu, Carbon encapsulation of high entropy alloy nanoparticles with extraordinary coercivity and saturation at room temperature, Part. Part. Syst. Char. 37 (2020), 2000137.

[7] M.Y. Rekha, N. Mallik, C. Srivastava, First report on high entropy alloy nanoparticle decorated graphene, Sci. Rep. 8 (2018) 8737.

[8] G. Popescu, B. Ghiban, C.A. Popescu, L. Rosu, R. Truscă, I. Carcea, V. Soare, D. Dumitrescu, I. Constantin, M.T. Olaru, et al., New tizrnbtafe high entropy alloy used for medical applications, IOP Conference Series: Mater. Sci. Eng. 400 (2018), 022049.

[9] T. Hirakawa, Y. Shimokawa, W. Tokuzumi, T. Sato, M. Tsushida, H. Yoshida, J. Ohyama, M. Machida, Multicomponent 3d transition-metal nanoparticles as catalysts free of pd, pt, or rh for automotive three-way catalytic converters, ACS. Appl. Nano. Mater. 3 (2020) 9097–9107.

[10] A. Serrà, E. Vallés, Advanced electrochemical synthesis of multicomponent metallic nanorods and nanowires: fundamentals and applications, Appl. Mater. Today. 12 (2018) 207–234.

[11] Y. Yang, B. Song, X. Ke, F. Xu, K.N. Bozhilov, L. Hu, R. Shahbazian-Yassar, M. R. Zachariah, Aerosol synthesis of high entropy alloy nanoparticles, Langmuir 36 (2020) 1985–1992.

[12] A. Mao, H. Xiang, X. Ran, Y. Li, X. Jin, H. Yu, X. Gu, Plasma arc discharge synthesis of multicomponent co-cr-cu-fe-ni nanoparticles, J. Alloy. Comp. 775 (2019) 1177–1183.

[13] M.A. Haq, N.S.A. Eom, N. Su, H. Lee, T.S. Kim, B.S. Kim, Powder interface modification for synthesis of core-shell structured cocrfeniti high entropy alloy composite, Appl. Surf. Sci. 506 (2020), 144925.

[14] K. Yao, L. Liu, J. Ren, Y. Guo, Y. Liu, Y. Cao, R. Feng, F. Wu, J. Qi, J. Luo, et al., High-entropy intermetallic compound with ultra-high strength and thermal stability, Scr. Mater. 194 (2021), 113674.

[15] X. Xu, Y. Du, C. Wang, Y. Guo, J. Zou, K. Zhou, Z. Zeng, Y. Liu, L. Li, High-entropy alloy nanoparticles on aligned electronspun carbon nanofibers for supercapacitors, J. Alloy. Comp. 822 (2020), 153642.

[16] N. Zhou, S. Jiang, T. Huang, M. Qin, T. Hu, J. Luo, Single-phase high-entropy intermetallic compounds (heics): bridging high-entropy alloys and ceramics, Sci. Bull. 64 (2019) 856–864.

[17] R. Sokkalingam, M. Tarraste, K.B. Surreddi, V. Mikli, V. Muthupandi, K. Sivaprasad, K.G. Prashanth, Powder metallurgy of al0.1cocrfeni high-entropy alloy, J. Mater. Res. 35 (2020) 2835–2847.

[18] Y. Yao, Z. Huang, P. Xie, S.D. Lacey, R.J. Jacob, H. Xie, F. Chen, A. Nie, T. Pu, M. Rehwoldt, et al., Carbothermal shock synthesis of high-entropy-alloy nanoparticles, Science 359 (2018) 1489–1494.

[19] S. Gao, S. Hao, Z. Huang, Y. Yuan, S. Han, L. Lei, X. Zhang, R. Shahbazian-Yassar, J. Lu, Synthesis of high-entropy alloy nanoparticles on supports by the fast moving bed pyrolysis, Nat. Commun. 11 (2020) 2016.

[20] B. Niu, F. Zhang, H. Ping, N. Li, J. Zhou, L. Lei, J. Xie, J. Zhang, W. Wang, Z. Fu, Sol-gel autocombustion synthesis of nanocrystalline high-entropy alloys, Sci. Rep. 7 (2017) 3421.

[21] F. Salemi, M.H. Abbasi, F. Karimzadeh, Synthesis and thermodynamic analysis of nanostructured cunicoznal high entropy alloy produced by mechanical alloying, J. Alloy. Comp. 685 (2016) 278–286.

[22] M. Bondesgaard, N.L.N. Broge, A. Mamakhel, M. Bremholm, B.B. Iversen, General solvothermal synthesis method for complete solubility range bimetallic and high-entropy alloy nanocatalysts, Adv. Func. Mater. 29 (2019), 1905933.

[23] M. Liu, Z. Zhang, F. Okejiri, S. Yang, S. Zhou, S. Dai, Entropy-maximized synthesis of multimetallic nanoparticle catalysts via a ultrasonication-assisted wet chemistry method under ambient conditions, Adv. Mater. Interfaces. 6 (2019), 1900015.

[24] Y. Chen, X. Zhan, S.L.A. Bueno, I.H. Shafei, H.M. Ashberry, K. Chatterjee, L. Xu, Y. Tang, S.E. Skrabalak, Synthesis of monodisperse high entropy alloy nanocatalysts from core@shell nanoparticles, Nanoscale. Horiz 6 (2021) 231–237.

[25] N.L.N. Broge, M. Bondesgaard, F. Søndergaard-Pedersen, M. Roelsgaard, B. B. Iversen, Autocatalytic formation of high-entropy alloy nanoparticles, Angew. Chem. Int. Ed. 59 (2020) 21920–21924.

[26] Z. Lin, J. Yue, L. Liang, B. Tang, B. Liu, L. Ren, Y. Li, L. Jiang, Rapid synthesis of metallic and alloy micro/nanoparticles by laser ablation towards water, Appl. Surf. Sci. 504 (2020), 144461.

[27] F. Waag, Y. Li, A.R. Ziefuß, E. Bertin, M. Kamp, V. Duppel, G. Marzun, L. Kienle, S. Barcikowski, B. Gökce, Kinetically-controlled laser-synthesis of colloidal high-entropy alloy nanoparticles, RSC. Adv. 9 (2019) 18547–18558.

[28] F. Okejiri, Z. Yang, H. Chen, C.-.L. Do-Thanh, T. Wang, S. Yang, S. Dai, Ultrasound-driven fabrication of high-entropy alloy nanocatalysts promoted by alcoholic ionic liquids, Nano. Res. (2021).

[29] T. Yang, Y.L. Zhao, B.X. Cao, J.J. Kai, C.T. Liu, Towards superior mechanical properties of hetero-structured high-entropy alloys via engineering multicomponent intermetallic nanoparticles, Scr. Mater. 183 (2020) 39–44.

[30] H. Peng, L. Hu, L. Li, W. Zhang, Ripening of l12 nanoparticles and their effects on mechanical properties of ni28co28fe21cr15al4ti4 high-entropy alloys, Mater. Sci. Eng. A. 772 (2020), 138803.

[31] J.C. Rao, H.Y. Diao, V. Ocelík, D. Vainchtein, C. Zhang, C. Kuo, Z. Tang, W. Guo, J. D. Poplawsky, Y. Zhou, et al., Secondary phases in alxcocrfeni high-entropy alloys: an in-situ tem heating study and thermodynamic appraisal, Acta. Mater. 131 (2017) 206–220.

[32] J.Y. He, H. Wang, H.L. Huang, X.D. Xu, M.W. Chen, Y. Wu, X.J. Liu, T.G. Nieh, K. An, Z.P. Lu, A precipitation-hardened high-entropy alloy with outstanding tensile properties, Acta. Mater. 102 (2016) 187–196.

[33] D. Zhao, L. Wang, L. Bo, D. Wu, Synthesis and thermoelectric properties of ni-doped zrcosb half-heusler compounds, Metals (Basel) 8 (2018) 61.

[34] A. Karati, M. Nagini, S. Ghosh, R. Shabadi, K.G. Pradeep, R.C. Mallik, B.S. Murty, U.V. Varadaraju, Ti2nicosnsb - a new half-heusler type high-entropy alloy showing simultaneous increase in seebeck coefficient and electrical conductivity for thermoelectric applications, Sci. Rep. 9 (2019) 5331.

[35] Q. Pan, Y. Wu, W. Zhong, F. Zheng, Y. Li, Y. Liu, J. Hu, C. Yang, Carbon nanosheets encapsulated nisb nanoparticles as advanced anode materials for lithium-ion batteries, Energy. Environ. Mater. 3 (2020) 186–191.

[36] X.-.M. Zheng, J.-.H. You, J.-.J. Fan, G.-.P. Tu, W.-.Q. Rong, W.-.J. Li, Y.-.X. Wang, S. Tao, P.-.Y. Zhang, S.-.Y. Zhang, et al., Electrodeposited binder-free sb/nisb anode of sodium-ion batteries with excellent cycle stability and rate capability and new insights into its reaction mechanism by operando xrd analysis, Nano. Energy. 77 (2020), 105123.

[37] H. Hou, X. Cao, Y. Yang, L. Fang, C. Pan, X. Yang, W. Song, X. Ji, Nisb alloy hollow nanospheres as anode materials for rechargeable lithium ion batteries, Chem. Commun 50 (2014) 8201–8203.

[38] V.S. Marakatti, S.C. Peter, Nickel–antimony nanoparticles confined in sba-15 as highly efficient catalysts for the hydrogenation of nitroarenes, New. J. Chem. 40 (2016) 5448–5457.

[39] P.P. Shanbogh, S.C. Peter, Low cost nano materials crystallize in the nias structure type as an alternative to the noble metals in the hydrogenation process, RSC. Adv. 3 (2013) 22887–22890.
[40] Y.-y. Qian, J. Yang, H.-r. Li, S.-q. Xing, Q. Yang, Solution-based synthesis of nisb nanoparticles for electrochemical activity in hydrogen evolution reaction, Chinese, J. Chem. Phys. 32 (2019) 373–378.
[41] Y. Xia, S. Bhattacharya, V. Ponnambalam, A.L. Pope, S.J. Poon, T.M. Tritt, Thermoelectric properties of semimetallic (zr, hf)cosb half-heusler phases, J. Appl. Phys. 88 (2000) 1952–1955.
[42] D.P. Young, P. Khalifah, R.J. Cava, A.P. Ramirez, Thermoelectric properties of pure and doped femsb (m=v,nb), J. Appl. Phys. 87 (2000) 317–321.
[43] B. Khan, H.A.R. Aliabad, I. Khan, S. Jalali-Asadabadi, I. Ahmad, Comparative study of thermoelectric properties of co based filled antimonide skutterudites with and without soc effect, Comput. Mater. Sci. 131 (2017) 308–314.
[44] B.C. Sales, D. Mandrus, R.K. Williams, Filled skutterudite antimonides: a new class of thermoelectric materials, Science 272 (1996) 1325.
[45] H. Kleinke, New bulk materials for thermoelectric power generation: clathrates and complex antimonides, Chem. Mater. 22 (2010) 604–611.
[46] N. Kazem, S. M. Kauzlarich Chapter 288 - thermoelectric properties of zintl antimonides. In Handbook On the Physics and Chemistry of Rare earths. Bünzli, J.-C. G., Pecharsky, V. K., Eds., Elsevier, 2016, pp. 177–208.
[47] G. Kieslich, C.S. Birkel, A. Stewart, U. Kolb, W. Tremel, Solution synthesis of nanoparticular binary transition metal antimonides, Inorg. Chem. 50 (2011) 6938–6943.
[48] J. Kashyap, H. Ahmed, D. Gujjar, L.P. Singh, H.C. Kandpal, P.C. Patel, Metal-arene driven reduction approach to synthesize binary antimonides: the case of xsb (x = fe, co and ni), Solid. State. Sci. 96 (2019), 105950.
[49] L. Kumari, W. Li, J.Y. Huang, P.P. Provencio, Nanosize transition metal antimonides, nisb and fesb2: solvothermal synthesis and characterization, J. Phys. Chem. C. 114 (2010) 9573–9579.
[50] D.A. Ogarev, S.A. Aitkhozhin, Y.S. Temirov, K.K. Palkina, K.A. Shchamkhalov, S. F. Marenkin, Bridgman growth of nisb single crystals, Inorg. Mater. 41 (2005) 1162–1165.
[51] P.C. Chen, X. Liu, J.L. Hedrick, Z. Xie, S. Wang, Q.Y. Lin, M.C. Hersam, V.P. Dravid, C.A. Mirkin, Polyelemental nanoparticle libraries, Science 352 (2016) 1565–1569.
[52] M.G. Naseri, E.B. Saion, H.A. Ahangar, M. Hashim, A.H. Shaari, Simple preparation and characterization of nickel ferrite nanocrystals by a thermal treatment method, Powder. Technol. 212 (2011) 80–88.
[53] I. Levin, Nist Inorganic Crystal Structure Database (icsd), National institute of standards and technology, Gaithersburg MD, 2018, p. 20899, https://doi.org/10.18434/M32147.
[54] M.F. Silva, L.A.S. de Oliveira, M.A. Ciciliati, M.K. Lima, F.F. Ivashita, D. M. Fernandes de Oliveira, A.A.W. Hechenleitner, E.A.G. Pineda, The effects and role of polyvinylpyrrolidone on the size and phase composition of iron oxide nanoparticles prepared by a modified sol-gel method, J. Nanomater. (2017), 7939727.
[55] S. Guo, E. Wang, One-pot, high-yield synthesis of size-controlled gold particles with narrow size distribution, Inorg. Chem. 46 (2007) 6740–6743.
[56] S. Mozaffari, W. Li, C. Thompson, S. Ivanov, S. Seifert, B. Lee, L. Kovarik, A. M. Karim, Colloidal nanoparticle size control: experimental and kinetic modeling investigation of the ligand–metal binding role in controlling the nucleation and growth kinetics, Nanoscale 9 (2017) 13772–13785.
[57] W. Li, Facile synthesis of monodisperse bi2o3 nanoparticles, Mater. Chem. Phys. 99 (2006) 174–180.
[58] C. Julien, G.A. Nazri, General overview of vibrational spectroscopy of layered transition-metal oxides, MRS Online Proceedings Library 548 (1998) 79–90.
[59] W. Zhang, Y. Zhang, Sci. China. Mater, Science China Earth Science (2018) 2–22.
[60] D. Ma, B. Grabowski, F. Körmann, J. Neugebauer, D. Raabe, Ab initio thermodynamics of the cocrfemnni high entropy alloy: importance of entropy contributions beyond the configurational one, Acta. Mater. 100 (2015) 90–97.
[61] Z.G. Zhu, K.H. Ma, Q. Wang, C.H. Shek, Compositional dependence of phase formation and mechanical properties in three cocrfeni-(mn/al/cu) high entropy alloys, Intermetallics 79 (2016) 1–11.
[62] R.-.Z. Zhang, M.J. Reece, Review of high entropy ceramics: design, synthesis, structure and properties, J. Mater. Chem. A. 7 (2019) 22148–22162.